Journal of Advanced Ceramics
2022, **11**(4): 523–531
https://doi.org/10.1007/s40145-021-0552-4
ISSN 2226-4108
CN 10-1154/TQ

Research Article

Enhanced electrical property of graphite/Al_2O_3 composite fabricated by reductive sintering of gel-casted body using cross-linked epoxy polymer

Yoshiaki FUNAHASHI[a], Yunzi XIN[b], Kunihiko KATO[b], Huu Hien NGUYEN[b], Takashi SHIRAI[a,b,*]

[a]*Department of Life Science and Applied Chemistry, Graduate School of Engineering, Nagoya Institute of Technology, Gokiso-cho, Showa-ku, Nagoya, Aichi 466-8555, Japan*
[b]*Advanced Ceramics Research Center, Nagoya Institute of Technology, Gokiso-cho, Showa-ku, Nagoya, Aichi 466-8555, Japan*

Received: May 30, 2021; Revised: October 8, 2021; Accepted: November 9, 2021

Abstract: In the present study, graphite/alumina composites are fabricated via reductive sintering of gel-casted green bodies with structurally controlled cross-linked epoxy polymers for the first time. The cross-linking degrees of polymers are tuned by the amount ratio of epoxy monomer/polyvinyl alcohol cross-linker utilized in gel-casting process. Superior electrical properties with respect to 5-fold enhanced electrical conductivity and 2-fold higher carrier mobility are successfully achieved in graphite/alumina composite fabricated from cross-linked epoxy polymer, whose phenomenon is attributed to the excellent conductive path in ceramic matrix established by highly uniform network with improved graphitization degree.

Keywords: ceramic composite; gel-casting; reductive sintering; cross-linking; electrical property; graphitization

1 Introduction

Nano-carbon/ceramic composites have attracted much attention due to higher electrical [1–6], thermal [7,8], and mechanical [9,10] properties than monolithic ceramics, and are the promising materials for electromagnetic interference shielding [1–3], lithium-ion battery [4–6], heat transfer, thermal energy storage [7,8], ballistic armor [9], and cutting tools [10]. Compared with other nano-carbon materials such as carbon nanotube [3,11,12], diamond [13,14], and graphite [15], graphene shows better electrical property owing to higher conductivity and larger contact area for building conductive path on ceramic matrix [16]. Recently, Momohjimoh *et al*. [17] reported the fabrication of ceramic matrix composite using carbon nanotube (CNT) as filler by sonication and ball milling and then consolidated by spark plasma sintering, and 1.01 S/cm electrical conductivity was prepared. Compared with CNT, by using graphene as filler, Hrubovčáková *et al*. [18] achieved 2.67 S/cm by spark plasma sintering of graphene coated alumina. Electrical conductivity-enhanced nano-carbon/ceramic composites are applied as anode for Li-ion battery [4–6,19], thermal interface materials [20,21], solar cells [22,23], and electromagnetic interference [24,25].

* Corresponding author.
E-mail: shirai@nitech.ac.jp

However, graphene is easily agglomerated by van der Waals (vdW) forces and its high specific surface area [26]. To achieve uniformly dispersion of graphene in solvent and ceramic matrix for reaching maximum capability as electrically conductive ceramics, further surface modification of graphene is required [27,28]. To overcome the drawbacks as mentioned in above conventional process, we have previously reported a novel fabrication process of nano-carbon/alumina composite via recombined process of gel-casting and reductive sintering [1,29–32]. Gel-casting is developed for the near-net shaping of ceramics with high green strength by utilizing the polymerization of gelation agents such as acrylamide, methacrylamide, and epoxy monomer [33–37] between ceramic powder. Instead of burning the polymer binder in an oxidative atmosphere [33–37], we conduct reductive sintering for pursuing a highly uniformed carbon component which consists of nanoscale graphitized carbon in the ceramic matrix with kept shape [1,29–32]. Additionally, we also demonstrated a superior p-type semi-conductive property with high hole mobility in nano-carbon/alumina composite fabricated from methacrylamide casted body [32].

In this study, nano-carbon/alumina composites are fabricated via reductive sintering of gel-casted green bodies with structurally controlled cross-linked epoxy polymers for the first time. The cross-linking degrees in different polymers were tuned by the amount ratio of epoxy monomer/polyvinyl alcohol (PVA) cross-linker, for perusing an enhanced electrical property of nano-carbon/alumina composite. With detailed characterization on the chemical structure and physical property as flow curve of polymer, relative density, microstructure, distribution, and structure of nano-carbon network, the effects of the cross-linked structure in polymer on the electrical properties with respect to electrical conductivity, carrier mobility, and density of the fabricated nano-carbon/alumina composite were systematically investigated. Against the utilization of toxic and air-sensitive monomer as methacrylamide in previous study, the non-toxic and air ambient available epoxy monomer, and facile structure tuning of polymer, as well as the superior electrical property in fabricated nano-carbon composite presented in current study opens a new strategy for the development of functional ceramic material.

2 Materials and method

2. 1 Sample preparation

The nano-carbon/alumina composite was fabricated by gel-casting and reductive sintering described as the following process, where bare polymer was also prepared as reference sample. Alumina powder (α-Al_2O_3, 99.48%, AL-160SG-4, Showa Denko K.K., Japan; median diameter D_{50} = 0.59 μm measured by laser diffraction particle size analyzer) was dispersed in distilled water with dissolved ammonium salt of polycarboxylate (Celuna D-305, Chukyo Yushi Co., Ltd., Japan) and PVA (polymerization degree = 500, Kanto Chemical Co., Inc., Japan) as dispersant and cross-linker for gelation, respectively. The slurry was well-mixed via ball-milled for 24 h at 60 rpm. Then, epoxy resin (poly glycidyl ether, Denacol EX-1610, Nagase ChemteX Corporation, Japan) as gelation agent was added into the well-mixed slurry and ball-milled for another 30 min. The slurry composition is shown in Table 1 excepting PVA. The amount ratio of epoxy/PVA was decided as 100/0, 80/20, and 60/40. In our pre-experiment, loading of PVA over 50% was not able to cast green body because of the high viscosity of slurry. The gelation was initiated by the addition of triethylenetetramine (TETA, Kanto Chemical Co., Inc., Japan) as a gelation initiator. Then degassed slurry was poured into mold and cured for 24 h. Demolded wet green bodies were then dried at 25 ℃ gradually, and relative humidity was altered from 90% to 60% for 5 d. For detailed study in cross-linking reaction between epoxy monomer and PVA, bare polymers without alumina powder loading were also prepared by altered epoxy monomer/PVA ratios of 100/0, 95/5, 90/10, 85/15, 80/20, 70/30, and 60/40. For reductive sintering process, green bodies were sintered at 1600 ℃ for 2 h in argon atmosphere and the obtained nano-carbon/alumina composites were ready for characterizations.

2. 2 Characterization

The chemical structure of bare polymers (without alumina powder) was analyzed by attenuated total reflection (ATR) method of an infrared Fourier transform (FT-IR, FT/IR-6600, JASCO, Japan). The rheological property of slurry was measured by a

Table 1 Compositions of the slurry

Material	Composition (wt%)
Al_2O_3 powder	77.2
Distilled water	19.8
Dispersant	0.7
Epoxy	2.3

rotary rheometer (Kinexus lab+, Malvern, UK). Shear rate of 0.1–100 s^{-1} was induced on slurry with a cone-and-plate geometry (cone angle = 4°, diameter = 40 mm). The relative density and the porosity were measured by the Archimedes method. The microstructure of sintered body was observed by scanning electron microscope (SEM, JSM-6010LA, JEOL). For analyzing element distribution on the surface of sintered body, energy dispersive X-ray spectroscopy (EDS) mapping was conducted. The amount of carbon contents in fabricated nano-carbon/alumina composite was measured by a commercial combustion infrared detection instrument (CS analyzer, LECO-CS884). The measurements were conducted on well-grounded powder. The carbon structure was investigated by Raman spectroscopy (in Via Raman microscope, Renishaw, UK) with a 532 nm laser.

The electrical properties were analyzed on a nano-carbon/alumina composite piece with a size of 10 mm × 5 mm × 3 mm by physical property measurement system (PPMS, Quantum Design, Inc., USA). The electrical conductivity was measured using a 4-probe method with the applied 1 mA current and temperatures of 200, 220, 240, 260, 280, and 300 K. The Hall measurement used a 5-probe method with the fixed current of 1 mA, and the applied magnetic field was set from −1.0 to 1.0 T. The mobility and the carrier density were calculated from the electrical conductivity and Hall resistivity.

3 Results and discussion

The chemical structure of the bare cross-linked epoxy polymers with different epoxy monomer/PVA ratio is analyzed by FT-IR spectroscopy, during which the spectra of epoxy monomer and PVA are also recorded, shown in Fig. 1. The assignments of all appeared peaks are summarized in Table 2. The broad band around 3400 cm^{-1} corresponding to O–H stretching vibration appears with C–O stretching vibration (peak L) of

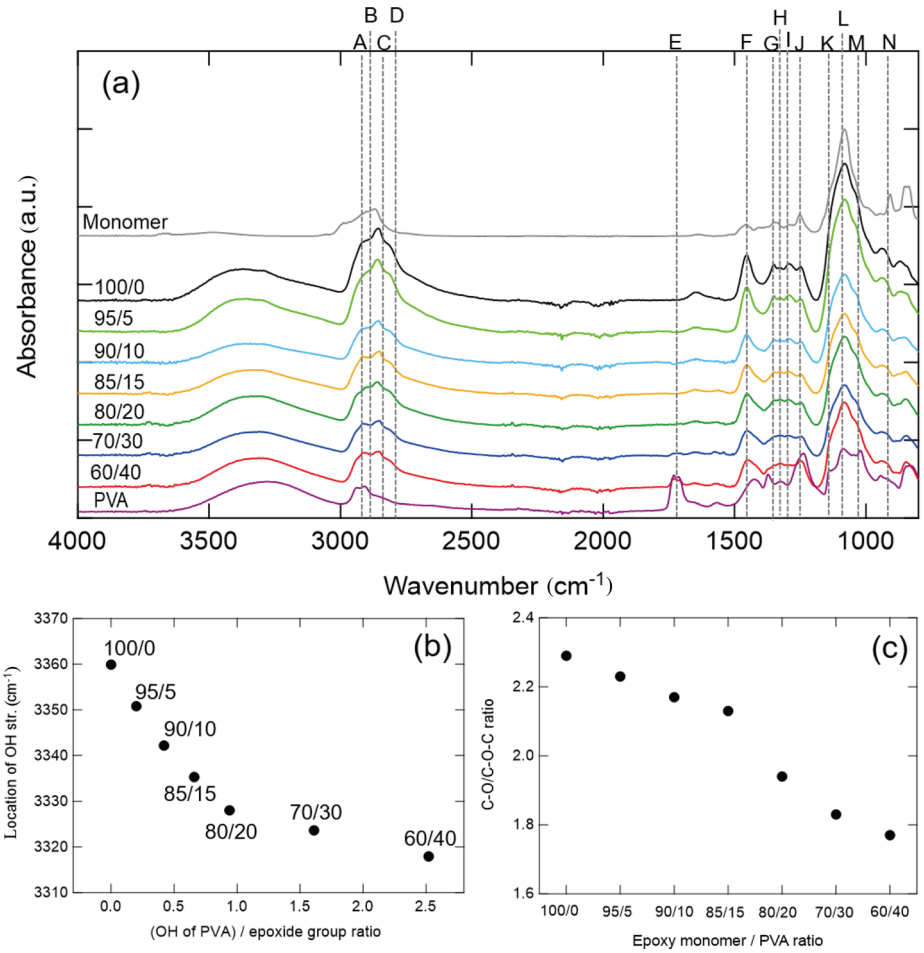

Fig. 1 (a) FT-IR spectra, (b) position of OH str. peak, and (c) absorbance of epoxy ring str. peak and C–O/C–O–C ratio of each bare polymer.

Table 2 Peak assignments in FT-IR spectra

Peak	Wavenumber (cm^{-1})	Spectral assignment	Ref.
A	2950	CH_3 asymmetric str.	[40]
B	2910	CH_2 asymmetric str.	[40]
C	2860	CH_3 symmetric str.	[40]
D	2820	CH_2 symmetric str.	[40]
E	1730	C=O str.	[41]
F	1455	CH_2 bend	[40]
G	1350	CH_3 bend	[40]
H	1325	C–H bend	[41]
I	1295	C–N str.	[42]
J	1250	C–O–C asymmetric str.	[43]
K	1125	C–O–C asymmetric str.	[43]
L	1085	C–O str.	[44]
M	1045	C–O–C symmetric str.	[43]
N	914	CH_2–O–CH epoxy ring, bend	[40]

secondary alcohol are assigned to the hydroxyl group in side chain of epoxy monomer, PVA, and reacted epoxide group in prepared polymers. Peaks A and C/G attribute to stretching and bending vibrations of CH_3, suggesting the existence of terminated CH_3 groups in each sample. Peaks B and F initialed from stretching and bending vibrations CH_2 along with peak H of C–H bending vibration indicate the hydrocarbon in all samples. The peak around 1295 cm^{-1} can be assigned as C–N bond, which is attributed to the trace amount of TETA. Peak N originated from epoxy ring is confirmed in epoxy monomer and disappears after PVA is induced which exemplifies that the polymerization of between epoxy monomer and PVA is progressed by cross-linking reaction. Peak D appears only in cross- linked epoxy polymers, which attributes to CH_2 in ring-opened epoxide groups. The peaks J, K, and M are assigned to C–O–C ether group, originated from the main chain of epoxy monomer and cross-linked structure of the polymers, while such C–O–C peak appearing in PVA with C=O (peak E) comes from acetic acid groups in incompletely saponified structure. As a further comparison, the peak of OH stretching vibration is plotted as a function of OH in PVA/epoxide group in monomer and illustrated in Fig. 1(b). The shifting to lower wavenumbers can be ascribed to the increased intermolecular hydrogen bonding resulting from increased amount of PVA in prepared epoxy polymer [39]. In advance, the C–O/C–O–C ratio is also summarized as a function of epoxy monomer/PVA ratio in Fig. 1(c). Such ratio decreases when more PVA is added, which suggests that the cross-linking reaction is preferentially proceeded [40]. In following parts, chemical and physical properties of nano-carbon/alumina composites fabricated with three selected epoxy monomer/PVA ratios of 100/0, 80/20, and 60/40 are discussed in details.

The flow curve of degassed slurries is exhibited in Fig. 2, which demonstrates that each slurry shows pseudoplastic fluid behavior and good castability can be expected. The viscosity of slurry increases with the increase of PVA amount, which shows good agreement with previous report [45]. As the relative density and open porosity of sintered body given in Fig. 2(b), the relative density decreases and open porosity increases as PVA amount increases. Generally, lower density affects to decreasing of electrical conductivity [46]. Nevertheless, electrical conductivity was increased in present study. This phenomenon is considered to be attributed to the pore inducing during gel-casting process with high viscosity slurry involving more PVA.

Figure 3 displays the SEM images of sintered bodies and corresponding EDS mapping results. It can be observed that the average grain size in nano-carbon/

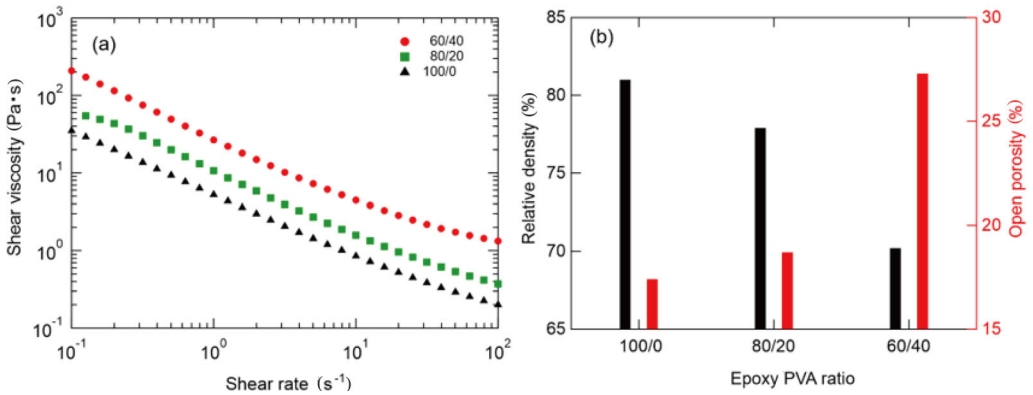

Fig. 2 (a) Flow curve of slurries, and (b) relative density and open porosity of sintered bodies.

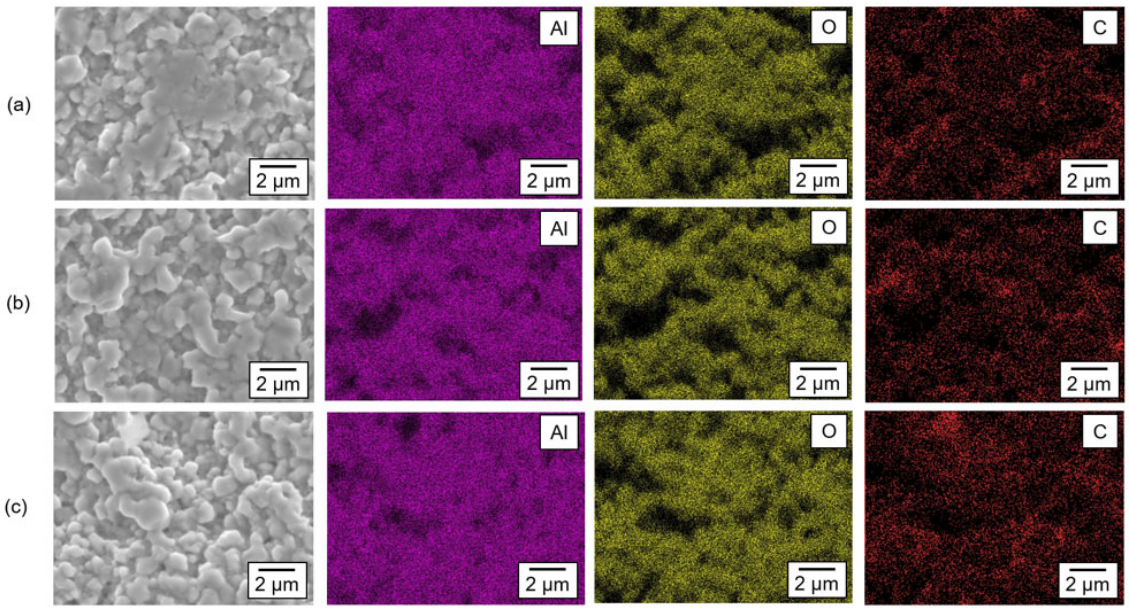

Fig. 3 SEM images of sintered bodies and EDS mapping results of carbon, aluminium, and oxygen of the obtained nano-carbon/ alumina composites fabricated by different epoxy/PVA ratios of (a) 100/0, (b) 80/20, and (c) 60/40.

alumina composites fabricated from epoxy monomer/ PVA ratios of 100/0, 80/20, and 60/40 decreases gradually. We suggest that the inhibition of grain growth from raw powder is attributed to the residual carbon, calculated from densities of Al_2O_3 (3.94 g/cm^3) and graphite (2.26 g/cm^3), that is, 1.15, 1.15, and 1.35 vol% for 100/0, 80/20, and 60/40 cases, respectively. As we previously mentioned, polymer formed in gel-casting transformed to nano-scale carbon coating on individual alumina grains [30]. The generation of highly uniform network in fabricated composites is also confirmed in EDS mapping of carbon. Regards to the result of relative density given in Fig. 2(b), it is also considerable that the decrement of relative density is probably originated from not only the pore induced in gel-casting of high viscosity slurry but also the inhibited sintering behavior caused by large carbon residue.

TEM images and FFT diffraction pattern are depicted in Fig. 4. The pore structure is generated with the increment of PVA amount in gel-casted green body, which is well correlated with open porosity results shown in Fig. 2(b). By focusing the TEM observation of Al_2O_3 surface, an expended image of Fig. 4(b) is illustrated in Fig. 4(d). Dark area with large contrast belongs to crystalline structure and is observed on Al_2O_3 surface. The observed interplanar distance of 0.341 nm is identified the same as the spacing of the (002) planes of graphite. Figure 4(c) is illustrated as enlarged Fig. 4(e) for further confirmation of the produced carbon structure between grain boundaries. The FFT pattern in Fig. 4(e) displays 2.92 nm^{-1} of the distance from central peak to diffraction peak as typical hexagonal crystalline structure of graphene. Figure 4(f) demonstrates the distribution of graphene and graphite in pore-involved composite fabricated in present study. As a result, we think percolation through the graphite/graphene network between Al_2O_3 grains and pore contributes to the electrical percolation and enhanced electronic conductivity even in 60/40 composite which contains more pores.

Next, the chemical structure of graphite network in fabricated composites is analyzed by Raman spectra, and the results are illustrated in Fig. 5. Three peaks appear at 1350, 1580, and 1620 cm^{-1}, which can be ascribed to D-band, G-band, and D'-band, respectively, are observed in all samples [47]. D-band is assigned to the edge of crystal and point defects of graphene, while G-band is ascribed to lattice vibration related to C–C (sp^2) bond. Furthermore, the defect of graphite-like structure is designated by D'-band [47,48]. The graphitization degree is investigated by *R*-value, refering to the intensity ratio between D-band and G-band (I_D/I_G) [48]. The higher *R*-value is ascribed to a less graphitized and more disordered carbon structure. To compare epoxy monomer/PVA ratio of 100/0 case with 80/20 and 60/40, *R*-value is decreased from 0.210 to 0.199 and 0.195, respectively. Thus, it can be concluded

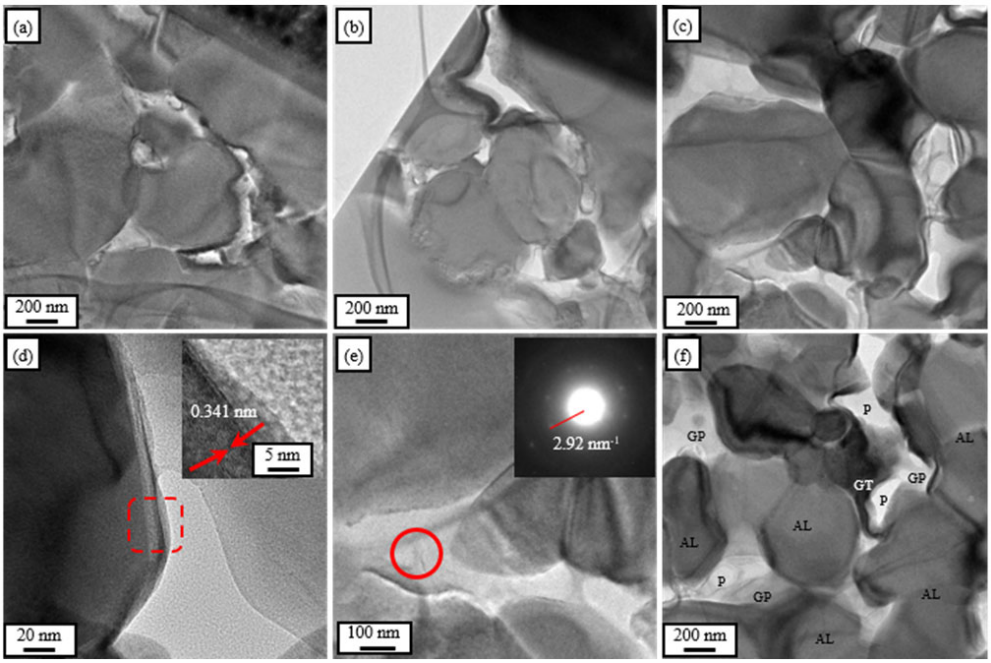

Fig. 4 TEM images of sintered bodies of the obtained graphite/alumina fabricated by different epoxy/PVA ratios: (a) 100/0, (b) 80/20, (c) 60/40, (d) extend Al_2O_3 surface of 80/20, (e) enlarge interparticle of 60/40, and (f) around pore of 60/40 (AL: Al_2O_3, P: pore, GT: graphite, and GP: graphene).

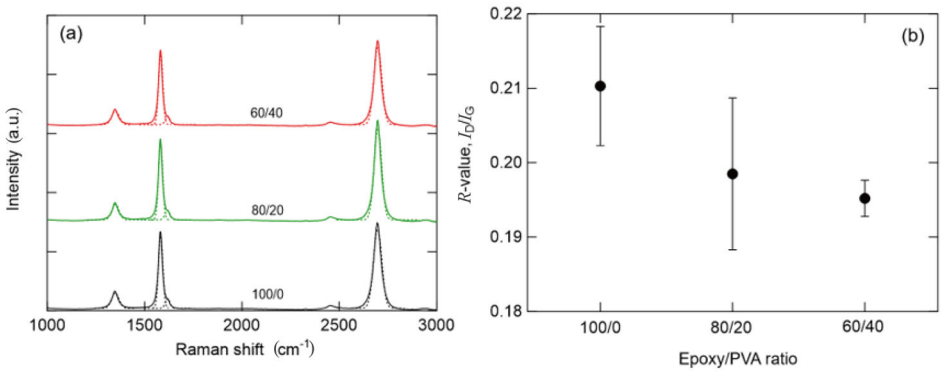

Fig. 5 (a) Raman spectra and (b) corresponding *R*-value of graphite/alumina composites.

that the graphitization degree is enhanced by the increase of PVA amount. It has been reported that low molecular weight volatile compositions are less generated from covalent bonding of cross-linked structure [49,50]. Therefore, we suggest the highly cross-linked structure in polymer generated by epoxy monomer/PVA ratio of 60/40 contributes to the improved graphitization degree. Meanwhile, it has been mentioned that the hydroxide group of PVA promotes the generation of aliphatic polyene structures under thermal degradation and such structure can form aromatic structure by Diels–Alder reaction and intra-molecular cyclization [51]. Thus, the excess PVA existed in the 60/40 case also plays a possible role in enhanced graphitization degree.

Electrical properties with respect to electrical conductivity, Hall resistivity, carrier mobility, and density of graphite/alumina composites are demonstrated in Fig. 6. As indicated in Fig. 6(a), the result demonstrates that graphite/alumina composite fabricated from epoxy monomer/PVA ratio of 60/40 exhibits the best electrical conductivity, which is attributed to the improved graphitization degree observed in graphite network formed by highly cross-linked polymer. The graphite network coated on alumina grains establishes a continuous conductive path along the grain boundaries, in despite of the different relative densities and the similar carbon content. The graphite generated on alumina particles and percolated around pore is proved

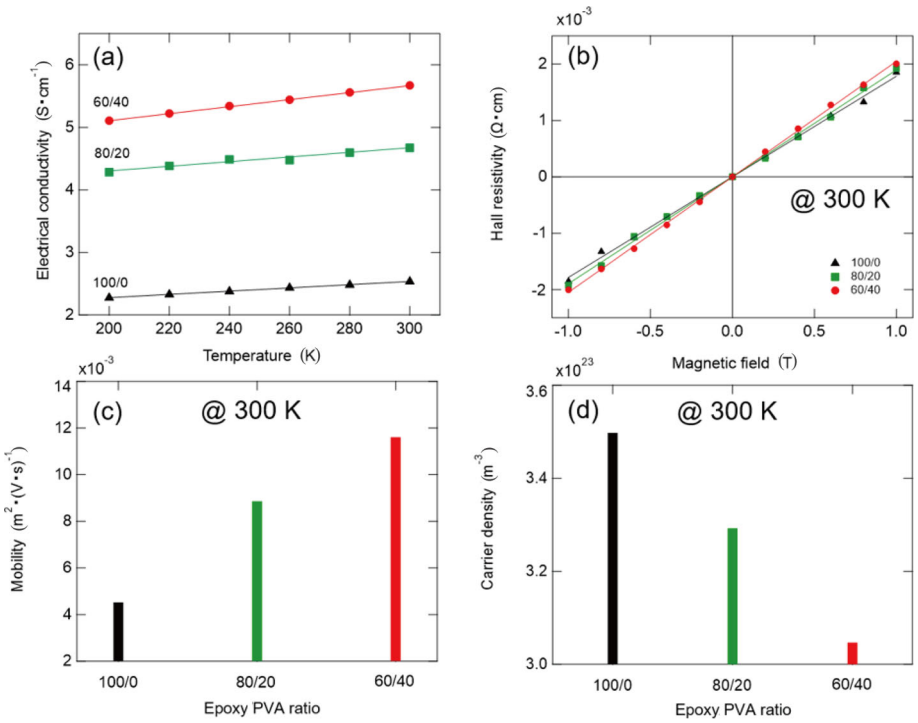

Fig. 6 Electrical properties of graphite/alumina composites: (a) temperature dependence of electrical conductivity, (b) Hall resistivity, (c) Hall mobility, and (d) carrier density.

by the results of TEM observation shown in Figs. 4(d) and 4(e). It is worth noting that the electrical conductivity of the fabricated graphite/alumina composite in this study is also significantly higher than those in the other conventional processes [52–55]. In addition, all the composites exhibit typical semi-conductive character since the electrical conductivity increases linearly with the increase of measuring temperature. The positive Hall resistivity observed in positive magnetic field designated in Fig. 6(b) demonstrates a p-type semi-conductive property of the obtained graphite/alumina composite. Our co-author has derived the origin for hole harvested p-type semi-conductive property, that is, the defects in graphite structure act as acceptors of π electrons, and doped aluminum atom in defect center provides excess hole carriers in graphite/alumina composite [32,56]. Regards to the results illustrated in Figs. 6(c) and 6(d), the carrier mobility is increased along the electrical conductivity in graphite/alumina composite fabricated from highly cross-linked polymer structure while the carrier density decreases due to the small amount of defective graphene. Therefore, it can be concluded that the superior electrical property with enhanced electrical conductivity and mobility is successfully achieved by reductive sintering of gel-casted bodies with selective structurally-controlled cross-linked epoxy polymers.

4 Conclusions

In this work, graphite/alumina composites were fabricated by gel-casting and reductive sintering, where the structure of polymer generated in gelation was controlled by altering the amount ratio of epoxy monomer/PVA. Highly cross-linked polymer structure was obtained with increased PVA amount, which contributes to the generation of graphite network with improved graphitization degree in later sintering process. Although increased slurry viscosity and inhibited sintering behavior lead to a decreased relative density in composite, the highly uniform carbon network coated on alumina grain was confirmed in all samples. In addition, enhanced electrical conductivity and carrier mobility were also successfully achieved in graphite/alumina composite fabricated from cross-linked epoxy polymer. The superior electrical property was attributed to the excellent conductive path established in ceramic matrix by uniform graphite network, with improved graphitization degree induced from polymer with highly cross-linked structure.

References

[1] Menchavez RL, Fuji M, Takegami H, *et al*. Electrically conductive gelcast porous alumina sintered under argon atmosphere. *Mater Lett* 2007, **61**: 754–756.

[2] Cao MS, Song WL, Hou ZL, *et al*. The effects of temperature and frequency on the dielectric properties, electromagnetic interference shielding and microwave-absorption of short carbon fiber/silica composites. *Carbon* 2010, **48**: 788–796.

[3] Lu MM, Cao WQ, Shi HL, *et al*. Multi-wall carbon nanotubes decorated with ZnO nanocrystals: Mild solution-process synthesis and highly efficient microwave absorption properties at elevated temperature. *J Mater Chem A* 2014, **2**: 10540–10547.

[4] Ding S, Luan D, Boey FY, *et al*. SnO_2 nanosheets grown on graphene sheets with enhanced lithium storage properties. *Chem Commun*: *Camb* 2011, **47**: 7155–7157.

[5] Wang D, Kou R, Choi D, *et al*. Ternary self-assembly of ordered metal oxide-graphene nanocomposites for electrochemical energy storage. *ACS Nano* 2010, **4**: 1587–1595.

[6] Wang D, Choi D, Li J, *et al*. Self-assembled TiO_2–graphene hybrid nanostructures for enhanced Li-ion insertion. *ACS Nano* 2009, **3**: 907–914.

[7] Zhou M, Bi H, Lin TQ, *et al*. Heat transport enhancement of thermal energy storage material using graphene/ceramic composites. *Carbon* 2014, **75**: 314–321.

[8] Zhou M, Lin TQ, Huang FQ, *et al*. Highly conductive porous graphene/ceramic composites for heat transfer and thermal energy storage. *Adv Funct Mater* 2013, **23**: 2263–2269.

[9] Alexander R, Murthy TSRC, Ravikanth KV, *et al*. Effect of graphene nano-platelet reinforcement on the mechanical properties of hot pressed boron carbide based composite. *Ceram Int* 2018, **44**: 9830–9838.

[10] Li ZL, Zhao J, Sun JL, *et al*. Reinforcement of Al_2O_3/TiC ceramic tool material by multi-layer graphene. *Ceram Int* 2017, **43**: 11421–11427.

[11] Yoshio S, Tatami J, Wakihara T, *et al*. Effect of CNT quantity and sintering temperature on electrical and mechanical properties of CNT-dispersed Si_3N_4 ceramics. *J Ceram Soc Jpn* 2011, **119**: 70–75.

[12] Athanasiou CE, Zhang HL, Ramirez C, *et al*. High toughness carbon-nanotube-reinforced ceramics via ion-beam engineering of interfaces. *Carbon* 2020, **163**: 169–177.

[13] Nguyen TP, Pazhouhanfar Y, Delbari SA, *et al*. Role of nano-diamond addition on the characteristics of spark plasma sintered TiC ceramics. *Diam Relat Mater* 2020, **106**: 107828.

[14] Nguyen VH, Delbari SA, Shahedi Asl M, *et al*. Microstructure-property correlation in nano-diamond and TiN added TiC-based ceramics. *Ceram Int* 2021, **47**: 449–460.

[15] Song LN, Xiao M, Li XH, *et al*. Short carbon fiber reinforced electrically conductive aromatic polydisulfide/expanded graphite nanocomposites. *Mater Chem Phys* 2005, **93**: 122–128.

[16] Huang YJ, Wan CL. Controllable fabrication and multifunctional applications of graphene/ceramic composites. *J Adv Ceram* 2020, **9**: 271–291.

[17] Momohjimoh I, Saheb N, Hussein MA, *et al*. Electrical conductivity of spark plasma sintered Al_2O_3–SiC and Al_2O_3–carbon nanotube nanocomposites. *Ceram Int* 2020, **46**: 16008–16019.

[18] Hrubovčáková M, Múdra E, Bureš R, *et al*. Microstructure, fracture behaviour and mechanical properties of conductive alumina based composites manufactured by SPS from graphenated Al_2O_3 powders. *J Eur Ceram Soc* 2020, **40**: 4818–4824.

[19] Pu FZ, Kong CC, Lv J, *et al*. CuO ultrathin nanosheets decorated reduced graphene oxide as a high performance anode for lithium-ion batteries. *J Alloys Compd* 2019, **805**: 355–362.

[20] An F, Li XF, Min P, *et al*. Highly anisotropic graphene/boron nitride hybrid aerogels with long-range ordered architecture and moderate density for highly thermally conductive composites. *Carbon* 2018, **126**: 119–127.

[21] Feng CP, Wan SS, Wu WC, *et al*. Electrically insulating, layer structured SiR/GNPs/BN thermal management materials with enhanced thermal conductivity and breakdown voltage. *Compos Sci Technol* 2018, **167**: 456–462.

[22] Mahmoudi T, Wang YS, Hahn YB. Stability enhancement in perovskite solar cells with perovskite/silver–graphene composites in the active layer. *ACS Energy Lett* 2019, **4**: 235–241.

[23] Chandrasekhar PS, Dubey A, Qiao QQ. High efficiency perovskite solar cells using nitrogen-doped graphene/ZnO nanorod composite as an electron transport layer. *Sol Energy* 2020, **197**: 78–83.

[24] Huang Y, Yasuda K, Wan C. Intercalation: constructing nanolaminated reduced graphene oxide/silica ceramics for lightweight and mechanically reliable electromagnetic interference shielding applications. *ACS Appl Mater Interfaces* 2020, **12**: 55148–55156.

[25] Chen C, Tan YQ, Han XC, *et al*. Enhanced electromagnetic interference shielding properties of silicon carbide composites with aligned graphene nanoplatelets. *J Eur Ceram Soc* 2018, **38**: 5615–5619.

[26] Papageorgiou DG, Kinloch IA, Young RJ. Mechanical properties of graphene and graphene-based nanocomposites. *Prog Mater Sci* 2017, **90**: 75–127.

[27] Liang AY, Jiang XS, Hong X, *et al*. Recent developments concerning the dispersion methods and mechanisms of graphene. *Coatings* 2018, **8**: 33.

[28] Liu YZ, Jiang XS, Shi JL, *et al*. Research on the interface properties and strengthening–toughening mechanism of nanocarbon-toughened ceramic matrix composites. *Nanotechnol Rev* 2020, **9**: 190–208.

[29] Takahashi M, Adachi K, Menchavez RL, *et al*. Fabrication of semi-conductive ceramics by combination of gelcasting and reduction sintering. *J Mater Sci* 2006, **41**: 1965–1972.

[30] Menchavez RL, Fuji M, Takahashi M. Electrically conductive dense and porous alumina with in-situ-synthesized nanoscale carbon networks. *Adv Mater* 2008, **20**: 2345–2351.

[31] Kato T, Shirai T, Fuji M, *et al*. Graphitization behavior of

polymer in the gelcasted alumina by sintering. *J Ceram Soc Jpn* 2009, **117**: 992–995.
[32] Xin YZ, Kumazawa T, Fuji M, *et al*. High hole mobility of a semi-conductive alumina/nano-carbon ceramic composite fabricated by gel-casting and reductive sintering. *J Eur Ceram Soc* 2019, **39**: 1730–1734.
[33] Young AC, Omatete OO, Janney MA, *et al*. Gelcasting of alumina. *J Am Ceram Soc* 1991, **74**: 612–618.
[34] Ha JS. Effect of atmosphere type on gelcasting behavior of Al_2O_3 and evaluation of green strength. *Ceram Int* 2000, **26**: 251–254.
[35] Sepulveda P, Binner JGP. Evaluation of the *in situ* polymerization kinetics for the gelcasting of ceramic foams. *Chem Mater* 2001, **13**: 3882–3887.
[36] Mao XJ, Shimai S, Dong MJ, *et al*. Investigation of new epoxy resins for the gel casting of ceramics. *J Am Ceram Soc* 2008, **91**: 1354–1356.
[37] Mao XJ, Shimai S, Dong MJ, *et al*. Gelcasting of alumina using epoxy resin as a gelling agent. *J Am Ceram Soc* 2007, **90**: 986–988.
[38] Silverstein RM, Bassler GC. Spectrometric identification of organic compounds. *J Chem Educ* 1962, **39**: 546–0.
[39] Shui T, Chae M, Bressler DC. Cross-linking of thermally hydrolyzed specified risk materials with epoxidized poly(vinyl alcohol) for tackifier applications. *Coatings* 2020, **10**: 630.
[40] Nikolic G, Zlatkovic S, Cakic M, *et al*. Fast Fourier transform IR characterization of epoxy GY systems crosslinked with aliphatic and cycloaliphatic EH polyamine adducts. *Sensors*: *Basel* 2010, **10**: 684–696.
[41] Geng Y, Wang GL, Cong YH, *et al*. Shear-induced nucleation and growth of long helices in supercooled isotactic polypropylene. *Macromolecules* 2009, **42**: 4751–4757.
[42] Yoshida S. Quantitative evaluation of an epoxy resin dispersion by infrared spectroscopy. *Polym J* 2014, **46**: 430–434.
[43] Vogel C, Siesler HW. Thermal degradation of poly(ε-caprolactone), poly(L-lactic acid) and their blends with poly(3-hydroxy-butyrate) studied by TGA/FT-IR spectroscopy. *Macromol Symp* 2008, **265**: 183–194.
[44] Ngono Y, Maréchal Y, Mermilliod N. Epoxy–amine reticulates observed by infrared spectrometry. I: Hydration process and interaction configurations of embedded H_2O molecules. *J Phys Chem B* 1999, **103**: 4979–4985.
[45] Billotte C, Fotsing ER, Ruiz E. Optimization of alumina slurry for oxide-oxide ceramic composites manufactured by injection molding. *Adv Mater Sci Eng* 2017, **2017**: 2748070.
[46] Mizusaki J, Waragai K, Tsuchiya S, *et al*. Simple mathematical model for the electrical conductivity of highly porous ceramics. *J Am Ceram Soc* 1996, **79**: 109–113.
[47] Bokobza L, Bruneel JL, Couzi M. Raman spectroscopic investigation of carbon-based materials and their composites. Comparison between carbon nanotubes and carbon black. *Chem Phys Lett* 2013, **590**: 153–159.
[48] Zólyomi V, Koltai J, Kürti J. Resonance Raman spectroscopy of graphite and graphene. *Phys Status Solidi B* 2011, **248**: 2435–2444.
[49] Levchik GF, Si K, Levchik SV, *et al*. The correlation between cross-linking and thermal stability: Cross-linked polystyrenes and polymethacrylates. *Polym Degrad Stab* 1999, **65**: 395–403.
[50] Grundy M, Ye ZB. Cross-linked polymers of diethynylbenzene and phenylacetylene as new polymer precursors for high-yield synthesis of high-performance nanoporous activated carbons for supercapacitors, hydrogen storage, and CO_2 capture. *J Mater Chem A* 2014, **2**: 20316–20330.
[51] Peng Z, Kong LX. A thermal degradation mechanism of polyvinyl alcohol/silica nanocomposites. *Polym Degrad Stab* 2007, **92**: 1061–1071.
[52] Qing YC, Wen QL, Luo F, *et al*. Temperature dependence of the electromagnetic properties of graphene nanosheet reinforced alumina ceramics in the X-band. *J Mater Chem C* 2016, **4**: 4853–4862.
[53] Çelik Y, Çelik A, Flahaut E, *et al*. Anisotropic mechanical and functional properties of graphene-based alumina matrix nanocomposites. *J Eur Ceram Soc* 2016, **36**: 2075–2086.
[54] Islam A, Mukherjee B, Sribalaji M, *et al*. Role of hybrid reinforcement of carbon nanotubes and graphene nanoplatelets on the electrical conductivity of plasma sprayed alumina coating. *Ceram Int* 2018, **44**: 4508–4511.
[55] Centeno A, Rocha VG, Alonso B, *et al*. Graphene for tough and electroconductive alumina ceramics. *J Eur Ceram Soc* 2013, **33**: 3201–3210.
[56] Xin YZ, Takeuchi Y, Shirai T. Influence of ceramic matrix on semi-conductive properties of nano-carbon/ceramic composites fabricated via reductive sintering of gel-casted bodies. *Ceram Int* 2021, **47**: 23670–23676.